remote sensing

MDPI

Article

The Morphology, Dynamics and Potential Hotspots of Land Surface Temperature at a Local Scale in Urban Areas

Jiong Wang [1,2,*], Qingming Zhan [1,2] and Huagui Guo [1,2]

Received: 4 November 2015; Accepted: 15 December 2015; Published: 30 December 2015
Academic Editors: Benjamin Bechtel, Iphigenia Keramitsoglou, Simone Kotthaus, James A. Voogt, Klemen Zakšek, Magaly Koch and Prasad S. Thenkabail

[1] School of Urban Design, Wuhan University, 8 Donghu South Road, Wuhan 430072, China; qmzhan@whu.edu.cn (Q.Z.); hgguo@whu.edu.cn (H.G.)
[2] Collaborative Innovation Center of Geospatial Technology, 129 Luoyu Road, Wuhan 430079, China
* Correspondence: jiongwang@whu.edu.cn; Tel.: 86-156-8067-2640

Abstract: Current characterization of the Urban Heat Island (UHI) remains insufficient to support the effective mitigation and adaptation of increasing temperatures in urban areas. Planning and design strategies are restricted to the investigation of temperature anomalies at a city scale. By focusing on Land Surface Temperature of Wuhan, China, this research examines the temperature variations locally where mitigation and adaptation would be more feasible. It shows how local temperature anomalies can be identified morphologically. Technically, the MODerate-resolution Imaging Spectroradiometer satellite image products are used. They are first considered as noisy observations of the latent temperature patterns. The continuous latent patterns of the temperature are then recovered from these discrete observations by using the non-parametric Multi-Task Gaussian Process Modeling. The Multi-Scale Shape Index is then applied in the area of focus to extract the local morphological features. A triplet of shape, curvedness and temperature is formed as the criteria to extract local heat islands. The behavior of the local heat islands can thus be quantified morphologically. The places with critical deformations are identified as hotpots. The *hotspots* with certain yearly behavior are further associated with land surface composition to determine effective mitigation and adaptation strategies. This research can assist in the temperature and planning field on two levels: (1) the local land surface temperature patterns are characterized by decomposing the variations into fundamental deformation modes to allow a process-based understanding of the dynamics; and (2) the characterization at local scale conforms to planning and design conventions where mitigation and adaptation strategies are supposed to be more practical. The weaknesses and limitations of the study are addressed in the closing section.

Keywords: LST; morphology; local scale; *hotspot*; yearly dynamics; urban area

1. Introduction

Cities possess a higher warming rate, and some are detected to be warming at twice the rate of the globe during the past 50 years [1]. Known as the Urban Heat Island (UHI) [2], the magnitude of the UHI could be up to 12 °C under calm and clear weather conditions [3–5]. Such a phenomenon has been documented since the 1800s [6]. The temperature has been analyzed in a more structured manner by recognizing the distinctive meteorological processes of urban areas. The UHI is further distinguished as Urban Canopy Layer (UCL) and Urban Boundary Layer (UBL) heat island [7]. Studies then have shown that temperature behavior is substantially influenced by land-use change [8], and suggested different heating contributions in terms of land-use change and other anthropogenic contributions

such as greenhouse gas emissions. Land surface composition management is highly recommended as a strategy for mitigating higher temperatures in urban areas [9].

1.1. The Land Surface Temperature

When the study of temperature focuses on investigating the Land Surface Temperature (LST) within the UCL, the UHI accordingly becomes the Surface Urban Heat Island (SUHI) [10]. The LST governs the energy balance within the UCL and modifies the air temperature of the lowest layer in an urban area [10,11]. It thus relates to microclimate in cities [12,13]. Remote sensing data from various satellite platforms with diverse spatial and temporal resolutions [14] is pervasively employed to monitor the LST [10,15,16]. These studies can be categorized into three groups: (1) investigation of LST pattern and its potential relation to urban factors; (2) studying the energy balance of urban surface; and (3) exploring the relationship between the LST and air temperature [10]. Within such a framework, few studies have extended beyond the first category [17]. The reason is that the relationship between the LST and urban factors is uncertain due to there being limited parameters describing the temperature pattern [18]. One milestone was characterizing the magnitude and spatial extent of the SUHI of Houston, Texas, USA through the application of the unimodal Gaussian surface to the fitting of the Advanced Very High Resolution Radiometer (AVHRR) image data [19,20]. An improved version was the application of the non-parametric kernel method to the LST and SUHI modeling in Indianapolis, Indiana, USA [21].

1.2. From Temperature Research to Planning Inefficiency

In contrast, planning and design professionals seem to have benefitted little from the preliminary city scale characterization of temperature patterns. This has been manifested in two ways: planning inefficiency and its consequences. Firstly, a number of cities are commonly reported to be without any form of regulation for temperature mitigation in terms of land surface management [22,23]. However, the impact of land surface has been stressed by the Intergovernmental Panel on Climate Change (IPCC) asserting that climate change may be due to persistent anthropogenic changes in land use [24]. Even at the local level, some climate action plans insufficiently addressed the problem by only considering the greenhouse gas emission [9]. Secondly, negative socio-economic consequences of the urban heat events have only become realized and addressed lately. For instance, over 15,000 people in France were killed during a summer Excessive Heat Event (EHE) in 2003 [25], while Arizona had the highest number of deaths due to heat exposure in the United States from 1993 to 2002 [26], and these numbers are expected to increase in the near future [27].

One significant discrepancy lies in the scope of current research of the temperature phenomenon and the level where mitigations are practically conducted. Conventional UHI studies have followed the large scale "urban-rural" dichotomy which is insufficient in capturing local diversity [28]. Planning professionals demand more straightforward guidelines at a local scale [29]. The other problem lies in the intrinsic dynamics of the LST. Daily and seasonal variations govern and constantly modify the local patterns of the LST. Characterizing the LST patterns becomes even more difficult. The dynamics may also complicate the land composition–phenomenon relationship, which in turn can further hinder the application of climate research results in the planning domain. These two issues stem from various problems such as lack of knowledge, communication, technical tools and prioritization, and unclear policy [30]. Derivation of more parameters to quantify temperature patterns is continuously encouraged [17,31].

1.3. This Research: Morphological Analysis of the LST

Keeping in mind the abovementioned facts, this study agrees with the proposition that characterizing the local LST patterns may be largely restricted by conventional parameters [18]. The research claims that the shape features such as cup, cap, and ridges should be brought into consideration as the LST is a spatial and geographical phenomenon. Previous studies [21] have only

implicitly shown that shape was the very first understanding of patterns, anomalies, and transitions at any scale. For example, the UHI on a temperature surface can be identified because of its convex shape [20,32] relative to the surroundings. Similar ideas should be applicable at a local scale.

This study employs morphological analysis to achieve two goals: (1) to provide a procedure for characterizing the LST dynamics at the local level; and (2) to propose prototype criteria to evaluate local LST anomalies for planning and mitigation. The dynamics may include how local LST varies daily, monthly and seasonally. Such dynamics can be categorized in terms of critical deformations. The locations with the most critical behaviors are denoted as *hotspots* and require planning actions with the highest priority. This responds to a simple question: where to start mitigation plans? It is believed that such achievements can facilitate the application of meteorological research findings in the planning domain. The research scale and level of priority determine the way in which mitigation and adaptation strategies are conducted.

Specifically, the 8-day MODerate-resolution Imaging Spectroradiometer (MODIS) data is used to represent the average daily LST variations for each month. The study starts with recovering the latent LST pattern from the raw MODIS data by using the Multi-Task Gaussian Process Model. The latent LST is the hidden continuous surface, which manifests the trend of temperature variation and can be disturbed by noise and missing observations [19,21]. The research then applies the Multi-Scale Shape Index to the latent LST patterns. The deformations are analyzed at their optimal scales. Critical transition types of the deformations are proposed. Sample *hotspots* are identified and then inspected in terms of their transition types as well as their relationships to the land surface composition. The details of the techniques are discussed in the following section.

2. Methodology

2.1. The Study Area

Wuhan, located in central China, is selected for a case study. It is the fifth most populous city of the country and characterized by its land surface heterogeneity. The water bodies scattered within and around the city highlight the diversity of its land composition. As shown in Figure 1, the extent of the study area is 46 × 36 km, which covers the entire downtown Wuhan and extends to the rural surroundings. The NW and SE coordinates are 30°43′53″N, 114°4′49″E and 30°24′0″N, 114°32′34″E, respectively. This coverage is sufficient to exhibit the land composition of the city.

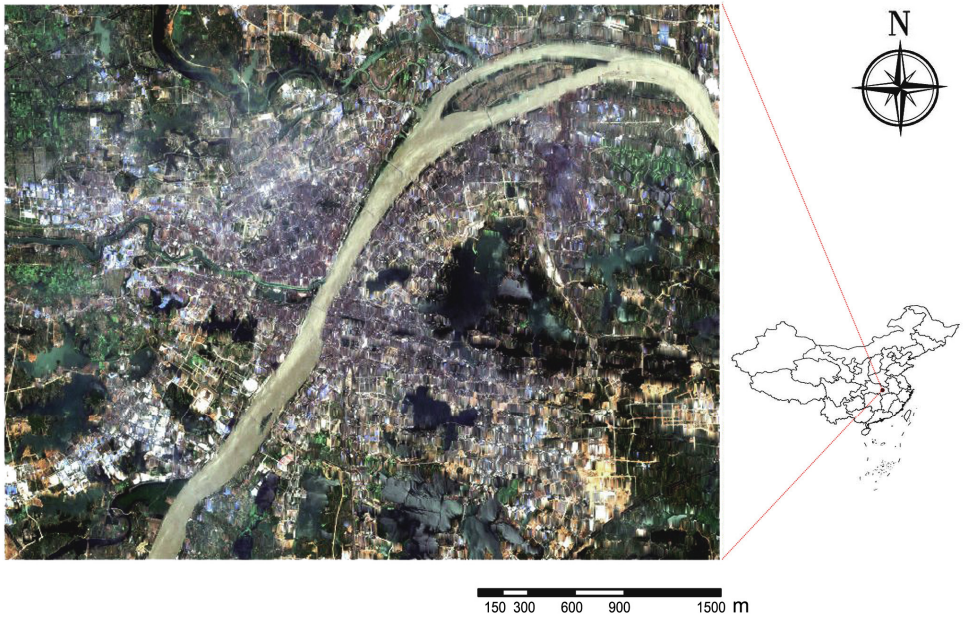

Figure 1. The study area represented by Landsat 7 ETM+ image (RGB) on 17 May 2012.

2.2. The Land Surface Temperature

Considering the potential diurnal and seasonal diversities, the LST data covers an entire year. For each month, one set of the MODIS/Terra (MOD11A2) and MODIS/Aqua (MYD11A2) V5 LST/E 8-Day L3 Global 1 km Grid products is used to represent the diurnal LST variation for the month. Thus, there are four images for each month. The MOD11A2 represents the LST at 10:30 and 22:30 local time, while the MYD11A2 is taken at 01:30 and 13:30 local time.

The data on a particular day is composed from the daily LST products MOD11A1 and MYD11A1 as the average values of clear-sky LSTs during the following eight-day period. The products are generated by using the generalized split-window LST algorithm [33]. According to the NASA Land Processes Distributed Active Archive Center, the daily products are validated through field campaigns and radiance-based validation studies. The accuracy of the LST data is better than 1 °C (0.5 °C in most cases) [34–36].

To ensure the products are desirable, each eight-day weather condition is examined. The acquiring dates of the selected data should include stable weather for at least two consecutive days during the eight days. The stability is determined by average wind speed and cloud cover overnight. It ensures that the weather is stable preceding and during the data acquirement. Weather stability is measured on the adapted Pasquill-Gifford scale [37–39]. It defines stability classes as D (Neutral), E (Slightly Stable), F (Moderately Stable), and G (Extremely Stable). The details are shown in Table 1.

Table 1. Selected image data and the corresponding weather information.

Month	MODIS 8-Day LST Data Dates (Julian Dates)	Consecutive Dates with Stable Weather during 8 Days	Average Cloud Cover	Average Wind Velocity	Adapted Pasquill-Gifford Stability Class
January	25 (025)	25–27	1.92/8	1.33 m/s	G
February	18 (049)	18–20	3.83/8	2.25 m/s	F
March	21 (081)	24–27	1.81/8	1.38 m/s	G
April	22 (113)	22–28	3.56/8	2.13 m/s	F
May	16 (137)	16–18	4.67/8	1.38 m/s	G
June	17 (169)	22–24	3.40/8	1.25 m/s	G
July	27 (209)	27–30	3.75/8	1.38 m/s	G
August	04 (217)	04–06	3.50/8	3.48 m/s	F
September	13 (257)	14–16	2.30/8	2.21 m/s	F
October	15 (289)	17–19	3.90/8	1.45 m/s	G
November	16 (321)	17–20	2.25/8	1.45 m/s	G
December	18 (353)	22–25	0.80/8	1.80 m/s	G
Notation	Adapted Pasquill-Gifford Class	<2 m/s	2–3 m/s	3–5 m/s	>5 m/s
	⩾4/8 Oktas	G	E	D	D
	<4/8 Oktas	G	F	E	D

2.3. The Latent Pattern of the Land Surface Temperature

As continuous information supports pattern analysis more effectively [40,41], the study hypothesizes the latent LST at the scale of the study area as a continuous and smooth surface [21]. The Multi-Task Gaussin Process (MTGP) model [42] as an extension of the Gaussian Process (GP) Model [43] is applied. The latent LST pattern of an image is extracted based upon both the image and temporally adjacent images. For example, the latent LST at 13:30 can be obtained from the image acquired at 13:30 in conjunction with its temporally closest neighbor image at 10:30. Using two images together will make the extraction to be more robust as illustrated later. These images with short time discrepancies are considered to be related tasks.

The model is applied for four reasons: (1) it removes noises and fills the missing pixels as curvature calculation can be sensitive to noises; (2) it recovers the latent LST as a continuous surface by populating the resolution by a factor of 2 where analysis of curvatures and shapes can be applied; (3) it is a flexible non-parametric model which controls local variations and maintains global diversity; and (4) it imposes no prior on the form of the function thus avoids human intervention of choosing models [43].

In the model, the observed data set D can be defined as $D = \{(\mathbf{x}_i, t_{ij}) \mid i = 1, \ldots, n, j = 1, \ldots, m\}$, where $\mathbf{x}_i$ is the *ith* location index in d dimensional space R^d (R^2 in this case). In this case, n is the number of pixels on one image, and m is the number of images used in the model. t_{ij} denotes observation made at location $\mathbf{x}_i$ in the *jth* image. Thus the vector $T = (t_{11}, \ldots, t_{n1}, t_{12}, \ldots, t_{n2}, \ldots, t_{1m}, \ldots, t_{nm})$ is noisy observations on multiple images. It is referred as Multi-Task Gaussian Process structure. Each task j corresponds to an image at a time with a series of n data points $(t_{1j}, \ldots, t_{nj})$. In this study, $m = 2$ as two images are used together each time. Instead of assuming the exact form such as $t = f(\mathbf{x}) + \varepsilon$, where $\varepsilon \sim N(0, \sigma_n{}^2)$ is the noise, the GP generalizes the function into an infinitely long vector $(f_1, \ldots, f_n)^{\mathrm{T}}$. Any finite set of the vector is jointly Gaussian. The model $f(\mathbf{x}) \sim \mathcal{GP}(m(\mathbf{x}), K^f K^{\mathbf{x}})$ is completely specified by the mean function $m(\mathbf{x})$ and covariance function. K^f is a covariance structure incorporating the inter-task information shared between tasks, and $K^{\mathbf{x}}$ is the covariance between measurement locations. In this research, the Automatic Relevance Determinant (ARD) is applied.

The prediction of any mean value $\overline{\mathrm{f}^*}$ of latent temperature is achieved through

$$\overline{\mathrm{f}_j^*} = m(x^*) + \left(k^f \otimes k^x(x^*, x)\right)^T \left(K^f \otimes K^{\mathrm{x}} + \Delta \otimes I\right)^{-1} (\mathbf{t} - m(\mathbf{X})) \tag{1}$$

in which $\otimes$ indicates the Kronecker product of matrices or vectors, K^f and $K^{\mathbf{x}}$ are covariance matrices of tasks and measurement locations, respectively. K^f is a column vector denoting the covariance among the task where inference is to be made and other tasks. $K^{\mathbf{x}}$ is the covariance between locations, and Δ is a diagonal matrix in which noise σ^2 are recorded [42].

At last, the optimal hyper-parameters of the ARD covariance function are learned by maximizing the log marginal likelihood as

$$\log \int P(\mathrm{t}|\mathbf{X}, \mathrm{f}) P(\mathrm{f}|\mathbf{X}) d\mathrm{f} = -\frac{1}{2}\mathrm{t}(\mathbf{K} + \sigma_n^2\mathbf{I})^{-1}\mathrm{t} - \frac{1}{2}\log\left|\mathbf{K} + \sigma_n^2\mathbf{I}\right| - \frac{n}{2}\log 2\pi \tag{2}$$

The data fit term $-\mathrm{t}(\mathbf{K} + \sigma_n^2\mathbf{I})^{-1}\mathrm{t}$ and complexity penalty term $\log\left|\mathbf{K} + \sigma_n^2\mathbf{I}\right|$ automatically adjust the trade-off between data fitting and model complexity. This is referred as William of Occam's principle of "Plurality should not be assumed without necessity" [43,44].

2.4. The Morphology of the Land Surface Temperature

The Multi-scale Shape Index (MSSI) [45] is an extension of Koenderink's Shape Index (SI) [46]. The MSSI evaluates shapes at the optimal scale. The evaluation thus contains two steps: (1) scale selection; and (2) the SI evaluation.

Evaluating the SI at a uniform level is unfavorable. The local variations of the latent LST are with different sizes and can be overlapped. The SI of each pixel should be calculated at its appropriate scale. The scale selection adopts the scale space [46,47] by projecting the LST pattern $f(s)$ to the scale space S through

$$S(f(s), \theta) = f(s) * k(s - u, \theta) = \int_0^s f(u) k(s - u, \theta) du \tag{3}$$

where $k(\,,\,)$ is the Gaussian kernel with varying smoothing magnitude θ centered at each location μ on the surface s. The characteristic scale of a point on the surface should best manifest the local feature at that point [47,48]. As the smoothing shifts the original point, the characteristic scale can be found in terms of the kernel size that produces the maximum normalized distance d traveled by a point in the scale space [45]. Since the distance traveled is along the kernel magnitude, the shifted distance caused by the kernel smoothing on an image surface is simply the difference between the original and the smoothed pixel values. The normalized distance is thus represented as

$$d = \frac{D(f, \theta)}{\theta} = \frac{||S(f, \theta) - f||^2}{\theta} \tag{4}$$

The optimal scale θ^* can be identified by the maxima of d through $(\partial D(f,\theta)/\partial\theta) = 0$. Briefly speaking, the zero derivative means that the local feature at the optimal scale should remain stable as the scale changes.

Then, the MSSI is the SI [46] evaluated at each point on a surface at the optimal scale. The SI of a point on a surface is a function of the principle curvatures at the point represented as

$$SI = \frac{2}{\pi}\arctan\frac{\kappa_2 + \kappa_1}{\kappa_2 - \kappa_1} SI \in (-1, 1) \quad (5)$$

where κ_1 and κ_2 ($\kappa_1 \geqslant \kappa_2$) are the principle curvatures. The principle curvatures can be easily evaluated from a noiseless continuous latent LST surface through eigenvalues of the Hessian matrix. The SI measures how a point varies relative to its surroundings as shown in Figure 2. The deformations are encoded within the interval (–1,1) The value indicates the extent of the deformation along principle curvatures. Typical shapes such as cup, rut, saddle, ridge, and cap can be measured along the interval. It thus captures both the geometry and magnitude.

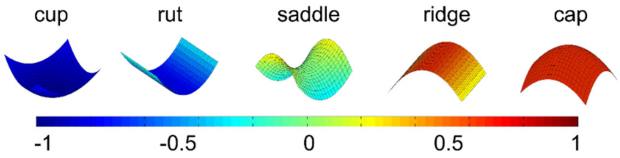

Figure 2. The surface morphology in the range of shape index.

However, the MSSI alone does not capture complete information on the latent morphology [46]. Objects with the same shape yet different sizes cannot be distinguished only by using the MSSI, thus the use of curvedness is also recommended [45]. The curvedness is calculated at the optimal scale θ^* based upon the principle curvatures through

$$curvedness = \sqrt{\frac{\kappa_1^2 + \kappa_2^2}{2}} \quad (6)$$

Thus, the MSSI, curvedness or optimal scale provide a complete profile of the underlying shape.

3. Results

3.1. Latent Pattern of the Land Surface Temperature

Taking the image data acquired at 13:30 on 27 July 2012 as an example, the latent pattern of the LST is recovered by using the MTGP model. The original and recovered LSTs are shown in Figure 3a,b, respectively. The missing pixels to the SE and SW corners of the image are all filled in the recovered image. Referring back to Figure 1, the infill reasonably characterizes the urban surface temperature with local bumps.

Figure 3c is a 1-dimensional illustration of how the MTGP model operates. The data is taken from the central column (Figure 3b) of the image. The model obtained based upon the "Occam's Razor" in Equation (2) controls the behavior of the latent LST. On one hand, the model should not be too simple to leave information as noise. The model controls the mean prediction to capture as much information in the observations as possible. On the other hand, the prediction prevents the model from over-fitting. It defines how quickly the nearby pixels may differ from each other. Thus, those pixels on the original image with large variations are considered to be noisy. This is the reason why local maxima and minima are suppressed. The model also gives the posterior covariance or uncertainty of the mean prediction. The observations are within two standard-deviations from the mean prediction of the latent LST. The overall RMSE between the mean prediction of the latent LST and observations of the image is 0.32 °C. It is acceptable because the difference is tolerated by the accuracy of the MODIS

LST product. Figure 3d gives the residuals produced by the difference between the mean predictions and corresponding observations in the entire image.

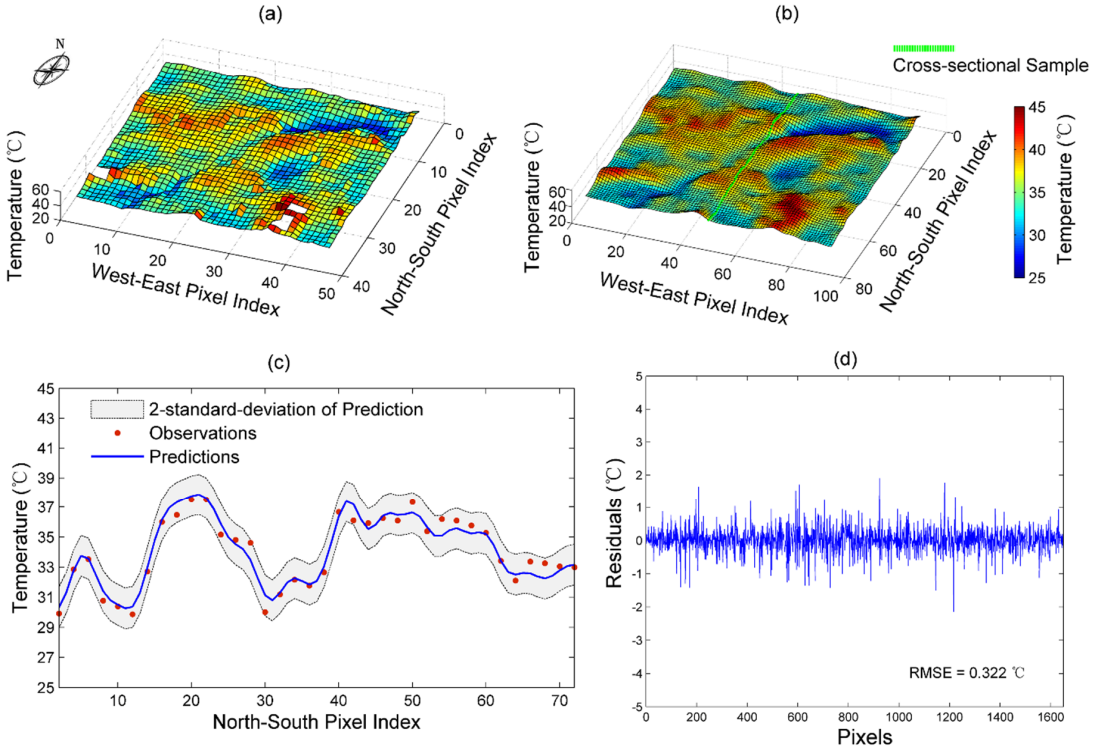

Figure 3. The latent LST recovered from the original observation acquired by satellite. (**a**) The original image at 13:30 on 27 July 2012; (**b**) The recovered continues latent LST pattern; (**c**) The difference between the observations and the latent LST; (**d**) The residuals due to recovery.

The modeling of the latent LST in other months produces even better results. As shown in Table 2, the RMSEs in each month are all within two standard deviations from the latent LSTs. During the cold season of December, January and February, the RMSEs are substantially smaller than the corresponding two standard deviations. It is potentially due to seasonal vegetation cover change and the lower surface temperature of the built environment. The reduction of vegetation cover makes the temperature behavior more homogenous within urban areas. The cold season makes the temperature difference between built environment and water bodies less prominent. Thus, the temperature variation within the study area is less dramatic which enables the model to capture the information more efficiently.

Table 2. The statistical summary of latent LST predictions for each month.

Time		01:30		10:30		13:30		22:30	
Month	**Calendar Date (Julian Date)**	**RMSE (°C)**	**Standard Deviation (°C)**	**RMSE (°C)**	**Standard Deviation (°C)**	**RMSE (°C)**	**Standard Deviation (°C)**	**RMSE (°C)**	**Standard Deviation (°C)**
January	25(025)	0.24	0.31	0.26	0.34	0.38	0.48	0.30	0.38
February	18(049)	0.49	0.91	0.30	0.41	0.64	0.40	0.64	0.62
March	21(081)	0.20	0.46	0.26	0.57	0.36	0.36	0.36	0.26
April	22(113)	0.30	0.55	0.46	0.37	0.44	0.55	0.44	0.39
May	16(137)	0.30	0.48	0.69	0.52	0.64	0.48	0.37	0.42
June	17(169)	0.34	0.34	0.78	0.43	0.64	0.34	0.27	0.46
July	27(209)	0.24	0.18	0.41	0.28	0.32	0.18	0.14	0.30
August	04(217)	0.25	0.27	0.35	0.41	0.21	0.27	0.21	0.33
September	13(257)	0.30	0.44	0.44	0.50	0.33	0.46	0.33	0.42
October	15(289)	0.32	0.27	0.22	0.26	0.19	0.43	0.19	0.43
November	16(321)	0.25	0.20	0.16	0.37	0.13	0.37	0.13	0.34
December	18(353)	0.23	0.37	0.49	0.32	0.26	0.32	0.28	0.31

In addition, it is necessary to check the reliability of the MTGP model. A robust test based upon a less desirable input image is conducted. To make the result comparable, the image in Figure 3a is used again as shown in Figure 4a. Pixels are artificially deleted. As missing pixels are concentrated in cloud-contaminated images, 500 randomly deleted pixels are weighted and distributed over the image. The missing values may, for example, be clustered to the west side of the image as shown in Figure 4b. These clustered and contiguous missing pixels resemble cloud-contaminated areas. This process is repeated 30 times, and the mean modeling result is shown in Figure 4c. The details in Figure 3b are visually well represented in Figure 4c. These two modeled surfaces are compared quantitatively in Figure 4d. The RMSE is 0.26 °C. This is acceptable in this research considering the tolerance of the standard deviation in Table 2. The robustness of the MTGP reflects the theory that information in related processes or tasks can be used to stabilize model performance. It has been addressed as to avoid *tabula rasa* modeling by sharing information across similar processes or tasks when information on one task is inadequate [42]. The inputs from multiple tasks help the model to make more confident predictions. While the choice of related tasks is based upon the prior knowledge of which tasks are related, the "Occam's Razor" would take effect to avoid over-fitting or under-fitting.

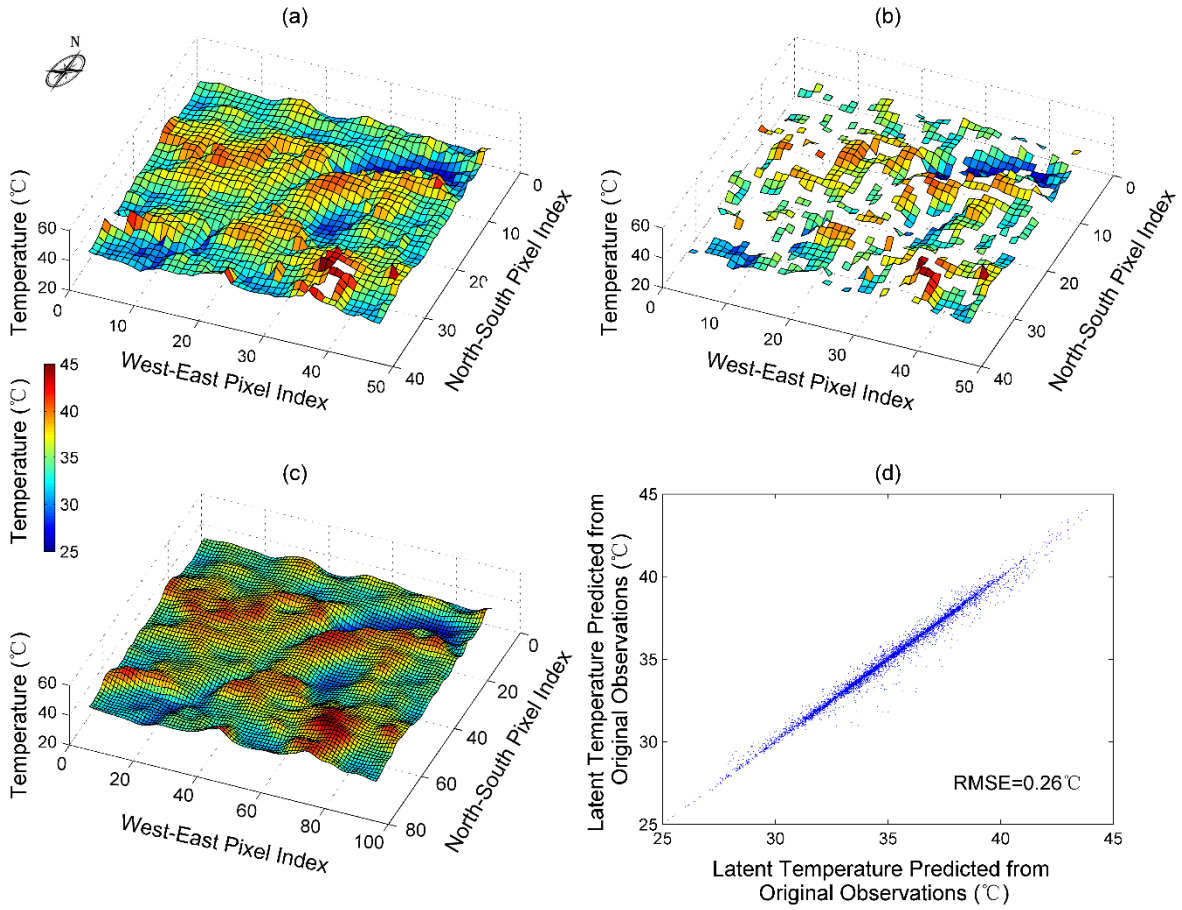

Figure 4. Robust test of the latent LST recovery. (**a**) The original image at 13:30 on 27 July 2012; (**b**) The manipulated image with more missing pixels; (**c**) The recovered continuous latent LST pattern; (**d**) Accuracy assessment of the recovered image by using the data recovered from the non-manipulated image.

3.2. The Morphology of the Latent LST

The continuous latent LST surface facilitates the calculation of principle curvatures and the MSSI. This section continues to use the image at 13:30 on 27 July 2012 for comparison. Figure 5a is the

result of applying Equation (5) directly with a uniform scale on the latent LST shown in Figure 3b. Some minimal variations are unnecessarily extracted. Figure 5b shows how the MSSI outlines the variations more holistically at a reasonable scale. It is clear that the water bodies and river are generally cooler. A reference place in the black circle also illustrates the industrial district temperature variation is treated as an integrity. Even though the MTGP takes care of the noise and missing values, the robustness of the MSSI can further ensure that local shapes are extracted properly. Figure 5c shows that with noise of 2 °C, the MSSI can be considered as stable. Such noise intensity ensures that the two standard deviations of the MTGP predictions and the MODIS data accuracy are both considered. The positive noise produces overestimated MSSI while the negative noise makes the MSSI slightly smaller. Still, the MSSI calculated from the noisy data remains almost unchanged relative to the one shown in Figure 5b. The average residual is 0.04.

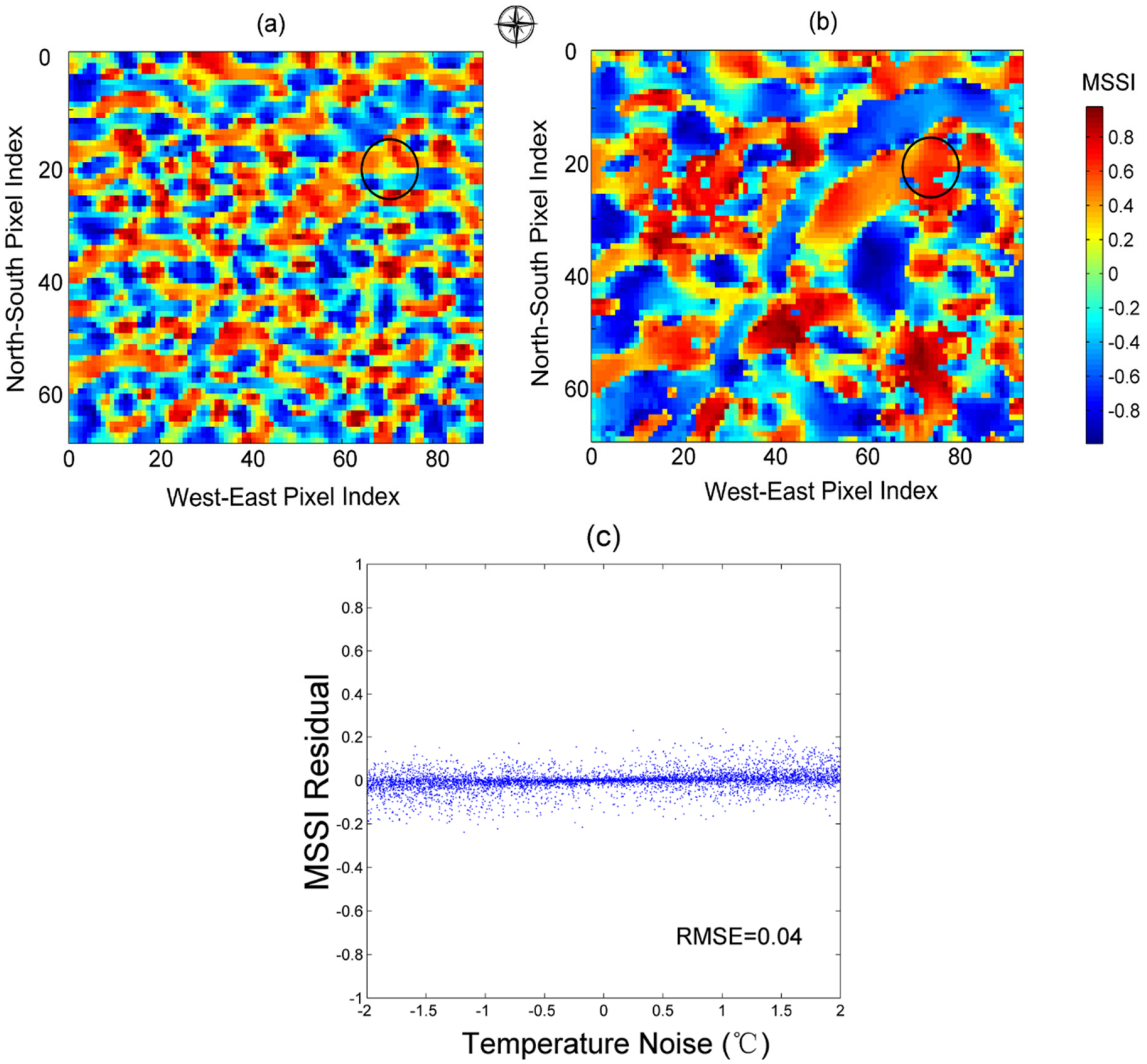

Figure 5. The Shape Index of the latent LST pattern. (**a**) The regular SI of the latent LST pattern at 13:30 on 27 July 2012; (**b**) The corresponding MSSI. The reference area is denoted by the black circle; (**c**) The robustness of the MSSI against noise.

As shown in Equation (6), the curvedness can also be calculated along with the principle curvatures at the optimal scale obtained through Equation (4). Besides the MSSI, Figure 6 further plots the MSSI, curvedness, scale and temperature of the data together. The bubbles represent the relative scale while the temperature is shown as the fourth dimension by color. There are five facts that are

worth emphasizing: (1) the pixels with globally higher temperature are more likely to be on local caps; (2) a few pixels with globally higher temperature are still locally cooler than the surroundings; (3) the values of the MSSI are clustered around 0.5 and −0.5, which reasonably reflects that the majority of the pixels are of the status between saddle and local extrema; (4) the curvedness is inversely proportional to the scale while the MSSI remains unchanged; and (5) the pixels with the same temperature and of the same shape can be with various curvedness or scales. An interesting feature in Figure 6 is that the MSSIs of the pixels with globally low temperature are clustered around −0.5. The reason is that these pixels are represented as dark blue bubbles and are located along the river, and their shape is thus characterized as rut with the MSSI value around −0.5.

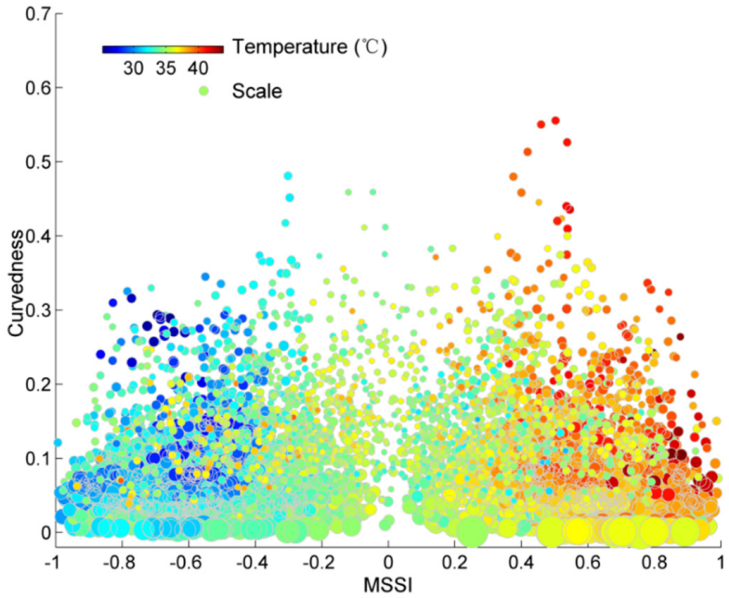

Figure 6. The relationships among the MSSI, curvedness, scale and temperature.

In summary, only curvedness and scale are inevitably related to each other. The temperature and shape are independent of other features.

3.3. The Spatial and Temporal Dynamics of the LST Morphology

As the LST patterns can be characterized by shape, curvedness or scale, this section continues to exhibit how the patterns can be differentiated spatially and temporally by these morphological indicators. For the data at 13:30 on 27 July, a target pixel is selected to show the details. The target pixel is located in a typical downtown area adjacent to a water body, and, thus, its LST pattern could be heterogeneous. Figure 7a shows the location of the target pixel along with its 15 × 15 neighbors.

For illustration, a column of pixels through the target pixel in the 15 × 15 sampling area is selected to demonstrate how the MSSI, curvedness and scale change through space. The selection thus contains 15 pixels as shown in Figure 7b. Figure 7c explores the details of the spatial dynamics of the pixels. The MSSI starts with 0.37 at the first pixel location, which indicates that the LST surface is relatively flat at the point. The MSSI rises and stays around 0.51 at the third and fourth pixel locations. It means that the LST surface at these points is bending along one direction and approximating the shape of a ridge. The MSSI continues rising and reaches 0.85 and 0.88 at the seventh and eighth pixel locations, respectively, which means that the LST at these points are nearly cap-shaped. These are visually clear in Figure 7b. Besides, the scale of the LST variation at the first few points stays around 4.55, which means that the underlying variation and shape are of a relatively uniform scale.

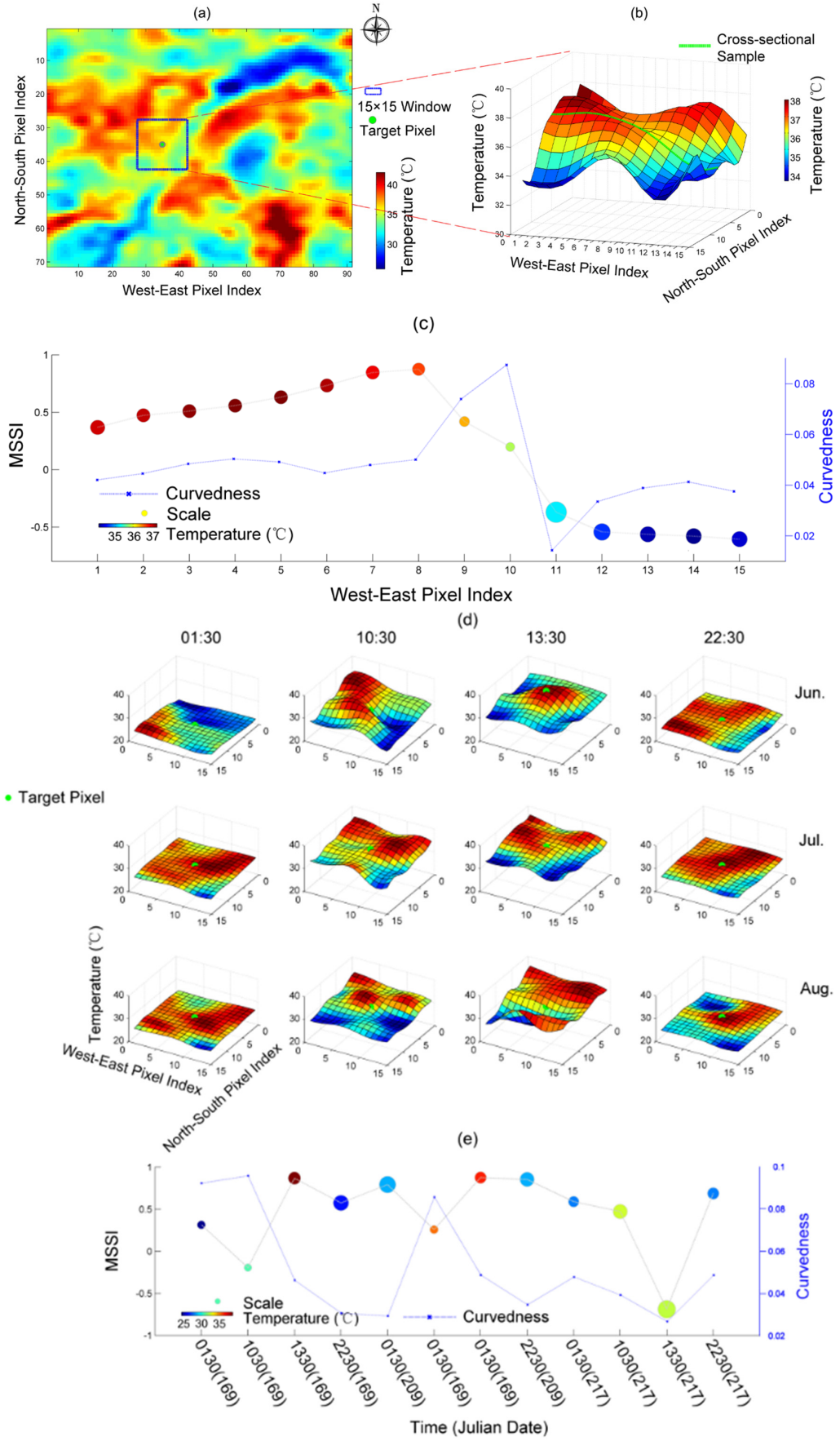

Figure 7. Spatial and temporal dynamics of sample LST. (**a**) The sample target of image at 13:30 July with its 15 × 15 neighbors; (**b**) The one-dimensional cross-sectional selection through the target; (**c**) The spatial dynamics of the cross-sectional sample; (**d**) The temporal temperature variation of the target relative to its neighbors through June, July and August; (**e**) The temporal dynamics of the target.

The MSSI drops dramatically at the ninth and 10th pixels indicating that the shape of the LST at these points becomes weak ridge-shaped, or is relatively fat and slightly bending in one direction. This is clearly shown in Figure 7b. The scale also drops quickly according to the sizes of the bubbles in Figure 7c, which indicates that the scale of the underlying LST at these locations is very small while the curvedness is strong. This is also prominent in Figure 7b where the LST slope is steep. It is different from the scales of the first few points where the scale is larger and the LST variation is smoother. The consistency between Figure 7b,c can be found for the rest of the samples.

The temporal LST dynamics of the target pixel is depicted in Figure 7d. The target is shown in the center of the sampling area. The morphological dynamics is highlighted by its 15×15 neighbors. The dynamics expands through June, July and August, which covers the warmer season. Thus, there are four images representing the average daily LST variation of each month. The target pixels on the slope of the first two images in Figure 7d produce the MSSIs of 0.31 and -0.19 indicating weak ridge and rut, respectively. The scales of these two target pixels are relatively small compared to the rest of the bubbles in Figure 7e, which means that the transition is sharp and the underlying LST surface at these points is with strong curvedness and bending fast.

Similar to Figure 7c, the MSSI, scale and temperature jointly quantify the temporal dynamics of the target pixel as shown in Figure 7e. While the latent temperature gradient is large at the target pixel, the scale of the underlying LST at target pixel is small indicating sharp transition. When the target pixel is close to large local cup or cap, the underlying LST at the target pixel becomes smooth and homogenous. Thus, the scale increases indicating weak curvedness. Besides the first two time points mentioned above, the latent LST at 10:30 in July is also of a small scale as temperature gradient is large at the target pixel. Specifically, as the target pixels of the images at 13:30 June, 22:30 July, and 22:30 August are just on the top of local bumps as shown in Figure 7d, they provide a better demonstration of scale/curvedness variation. As shown in Figure 7e, the MSSIs reasonably characterize these particular targets as caps. The scale of the target at 13:30 June is 4.55. The scale then changes to 6.00 at 22:30 July and finally turns to 3.96 at 22:30 August. This process is visually evident in Figure 7d where the size of the local LST bump varies accordingly. The details of the parameters are listed in Table 3.

Table 3. The spatial and temporal dynamics of samples.

Dynamics	Pixel Index	MSSI	Relative Scale (Pixels)	Temperature (°C)	Curvedness
Sample Spatial Dynamics (13:30 on 27 July)	1	0.37	5.22	37.10	0.04
	2	0.47	4.55	37.16	0.05
	3	0.51	4.55	37.29	0.05
	4	0.56	4.55	37.37	0.05
	5	0.63	4.55	37.34	0.05
	6	0.73	4.55	37.21	0.04
	7	0.85	4.55	37.01	0.05
	8	0.88	3.96	6.73	0.05
	9	0.42	2.61	36.35	0.07
	10	0.20	1.98	35.82	0.09
	11	−0.37	10.45	35.19	0.01
	12	−0.54	6.89	34.58	0.03
	13	−0.56	6.00	34.15	0.04
	14	−0.58	6.00	34.03	0.04
	15	−0.61	6.00	34.26	0.04
Sample Temporal Dynamics	1	0.31	1.98	24.25	0.09
	2	−0.19	1.72	30.79	0.09
	3	0.87	4.55	39.18	0.05
	4	0.57	6.89	26.24	0.03
	5	0.79	7.92	28.52	0.03
	6	0.26	1.98	35.65	0.08
	7	0.88	3.96	36.73	0.05
	8	0.85	6.00	28.58	0.03
	9	0.59	3.45	27.76	0.05
	10	0.47	6.00	32.68	0.04
	11	−0.69	9.09	32.61	0.03
	12	0.69	3.96	27.96	0.05

3.4. Identification of the Potential Hotspots

According to the results in Sections 3.2 and 3.3 the variation of the LST pattern can be differentiated morphologically by shape, scale and curvedness, while scale and curvedness depend on each other. It is reasonable to include temperature as an additional criterion to analyze the LST at different levels. A triplet of criteria is formed to select the target LST pattern as shown in Figure 8a. Thus, the criteria are the MSSI, curvedness or scale, and temperature threshold. The triplet can be used to select the LST with a special behavioral pattern at a particular time, or to track the behavior of the LST through time instead of focusing on static local UHI. Specifically, the triplet can be used to extract those places with particular behaviors over days and months. For example, as shown in the center of the diagram in Figure 8, those places that maintain a local heat island for a whole day at each of the four time points can be of great interest to planners or designers who are concerned with mitigation of UHIs. Following the conventions of Sections 3.1 and 3.2 the robustness of the triplet is tested and shown in Figure 8b. It shows how the triplet locates the pixels with potential noise. Five random pixel locations are selected along with their triplets of MSSI, curvedness and temperature. These triplets are used to locate the most similar pixels in the noisy data. Even though the locations in the noisy data can be different from the original ones with a discrepancy of one or two pixels, most pixels are located correctly. It is clear that larger discrepancy values are clustered toward higher noise intensity. The average discrepancy is 0.38 pixels which is at the sub-pixel level.

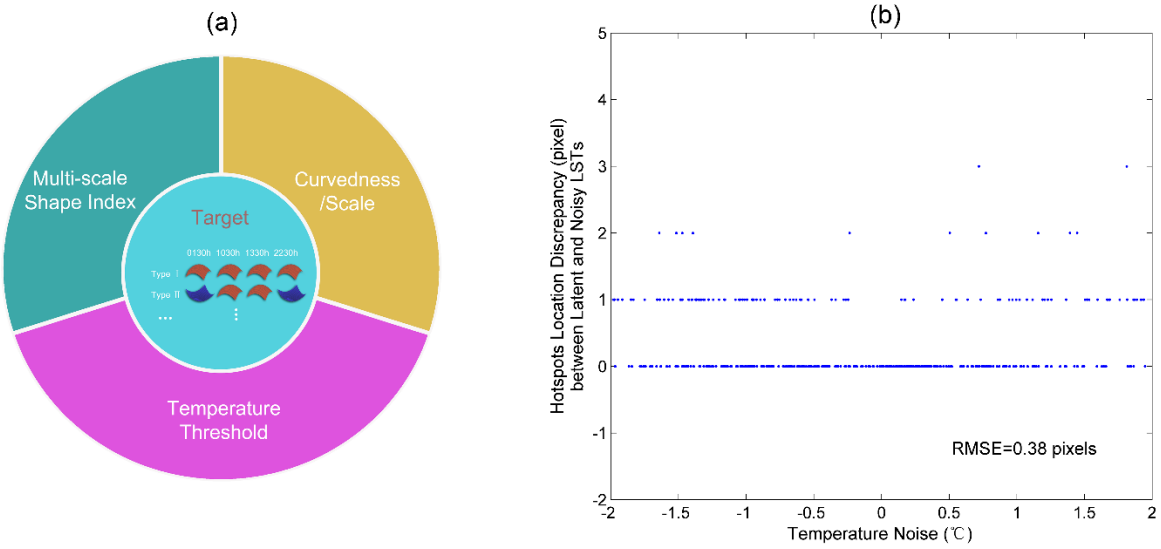

Figure 8. (**a**) The triplet criteria for analyzing the dynamics of the LST; (**b**) The robustness of locating pixels with the triplet criteria.

Figure 9 illustrates how local *hotspots* that satisfy particular criteria can be extracted. Again, a column of pixels is randomly selected for the simplicity of illustration as shown in Figure 9a. In this example, the curvedness is used instead of the scale. The *hotspots* are defined as: (1) those pixels with temperature higher than a particular global threshold; (2) the pixels are also hotter than the surroundings such that the MSSI should be positive; and (3) the curvedness is large which means that the variation is relatively intense. For illustration, the temperature threshold is set to be the median value of 34.87 °C. To include local high temperature on the ridge, the minimum MSSI is set to be 0.50. The minimum curvedness is also set to be the median value of this image, which is 0.05. The threshold can be applied similarly by using other statistics of the criteria, such as mean or standard deviations.

The temperature threshold as one of the criteria is shown in Figure 9b along with the temperature profile. There are six potential local *hotspots* while the sixth one is screened by the temperature threshold. The MSSI and curvedness as the other two criteria are shown in Figure 9c.

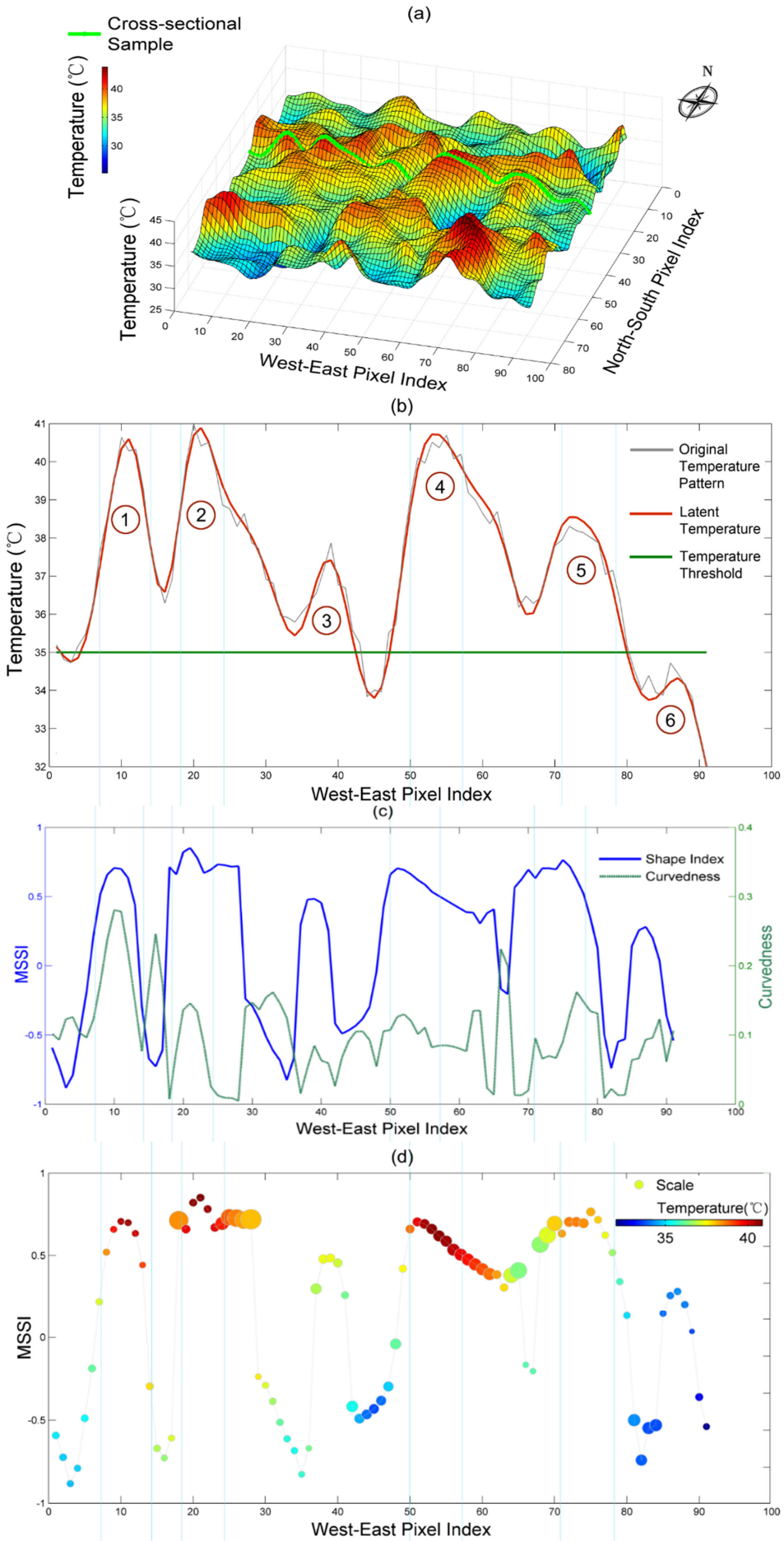

Figure 9. *Cont.*

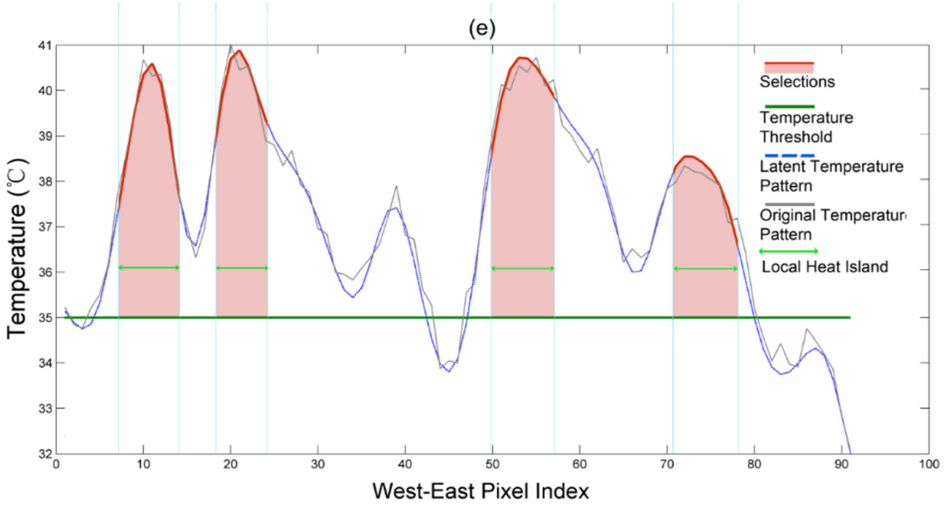

Figure 9. Selection of LST pixels satisfies MSSI > 0.50, curvedness > 0.05, and temperature > 34.87 °C. (**a**) The sample column from the latent LST at 13:30 July; (**b**) The temperature profile of the latent LST sample superimposes over the original noisy data while the temperature threshold is also shown; (**c**) The MSSI and curvedness of the sample used as criteria; (**d**) The scale is also shown along the MSSI; (**e**) The resulting selection.

At least two aspects in the results reflect the strength of the criteria. Firstly, they show that part of the second potential *hotspot* is screened by the curvedness. As the *hotspot* is visually skewed to the right, the part to the right side is estimated to be of a larger scale and weaker curvedness. Comparing the MSSIs of the first two *hotspots*, it is clear that the underlying LST variation of the first one is more homogeneous while the second one might be a mixture of two or more bumps with different curvedness or scales. The second one is thus evaluated at different scales with various shapes and curvedness. The values are consistent with the two-dimensional information in Figure 9a. A similar situation can be found in the four *hotspots*, which are also visually skewed to the right. Secondly, while the third potential *hotspot* meets the temperature threshold and curvedness criteria, it is estimated as a weak local ridge as shown in Figure 9a, and its MSSI fails to reach 0.5. Figure 9e highlights the *hotspots* that meet the selection criteria. For completeness of information, the scale is also shown in Figure 9d along with the MSSI.

3.5. The Yearly Dynamics of the Hotspots-Land Surface Composition Relationship

To further show how the triplet illustrated in Figure 8 can be applied to examine the yearly *hotspots* dynamics, it is necessary to focus on those places that are constantly locally high for a year. For illustration, this section focuses on the places that maintain a local high on an average monthly diurnal basis. For a particular place, it means that at all four time points of 01:30, 10:30, 13:30, and 22:30, the temperature pattern represents an average monthly diurnal pattern constantly maintaining a local *hotspot*. It is shown as type I *hotspot* illustrated in Figure 8. Thus, this type is determined by temporal behavior. For each of the 12 months of a year, only the places considered as a local *hotspot* at all the five time points are considered as type I *hotspots* for a month. A place can be a type I *hotspot* with a frequency of up to 12 throughout a year. In addition, how the land surface composition affects the scale or curvedness of the *hotspots* is also considered. Only the MSSI of criteria is fixed. Thus, type I *hotspots* means that each month the MSSIs of the pixels are significantly greater than 0 at all the time points, and the pixels can be of any scale or curvedness at any temperature level. Specifically, to ensure that the MSSI criteria is significantly greater than 0, a statistical examination is conducted based upon the yearly distribution of the MSSI. A mixture of 3 Gaussian is applied by assuming the pixels are clustered around 0, 0.5 and −0.5. The model uses Expectation Maximization to estimate the fitting parameters. After running the model 30 times, the mean fitting parameters are shown in Table 4. Thus, the pixels

with MSSI over 0.22 can be considered to be significantly warmer than their surroundings at 95% confidence level.

Table 4. The average statistical summary of the MSSI distribution for all the image data.

Gaussian Distribution Parameters	μ	σ	2 × σ	2 × σ Greater than 0
3-Gaussian-Distribution Mixture	0.02	0.10	0.20	0.22
	0.51	0.04	0.08	\
	−0.52	0.05	0.09	\

The type I *hotspots* are extracted from each month based upon the four images from that month. Figure 10a shows the distribution and frequency of the type I *hotspots* for the 12 months. The *hotspots* are scattered across the whole study area, however, a higher number of type I *hotspots* is found to be clustered within built-up areas. The area with the highest frequency appears to be the industrial district in the NE corner of the study area. The temperature pattern of the district is largely influenced by anthropogenic heat emission and maintains a local high all day long for nearly a whole year. The highest frequency is 10, which means that the pixel is considered as part of a local high at all four time point for 10 months. In addition, to show seasonal dynamics, Figure 10b–e maps the distribution and frequency of the *hotspots* in December~February (DJF), March~May (MAM), June~August (JJA), and Septermber~November (SON), respectively. Specifically, according to Figure 10c,d, the urban areas are more likely to be type I *hotspots* during warmer seasons of MAM and JJA. In the cold season of DJF, the water bodies are generally warmer than the rest of the areas in this case study, and the water bodies are more likely to be type I *hotspots* as shown in Figure 10b. In contrast, less type I *hotspots* can be found during the cooler season of SON as shown in Figure 10e. It means that few places in the study area can maintain a local *hotspot* for a whole day during this season.

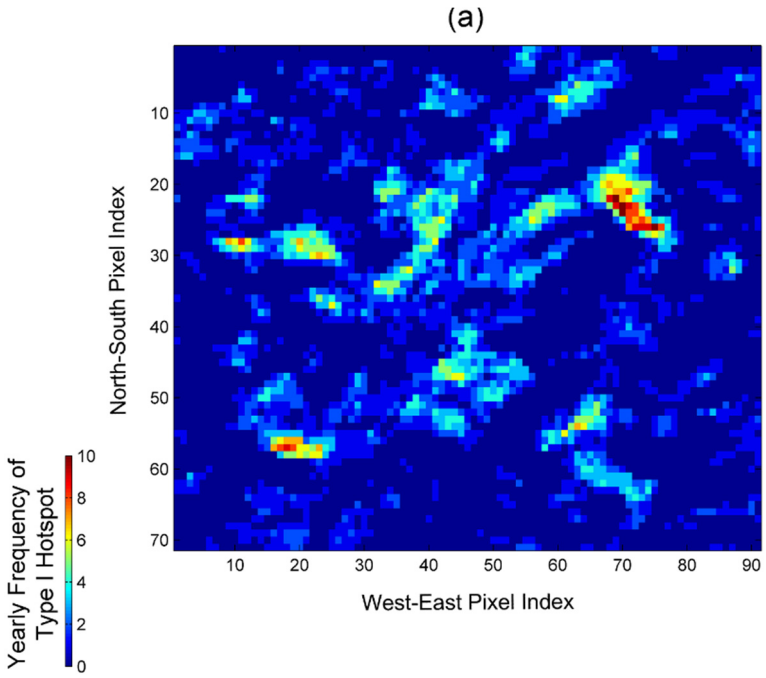

Figure 10. *Cont.*

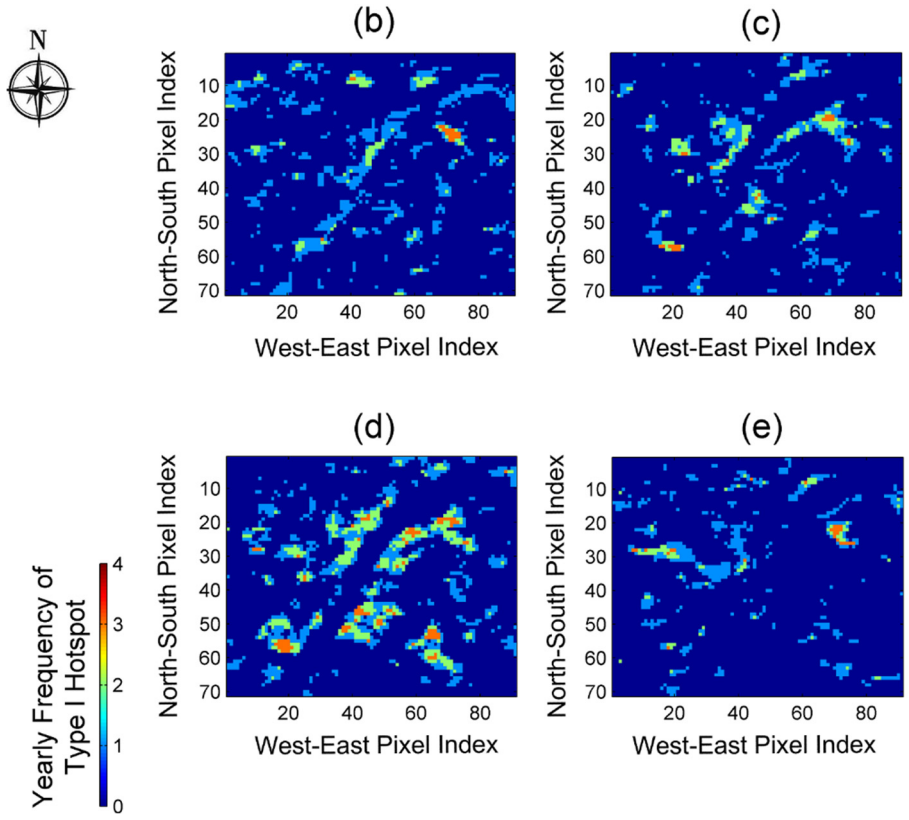

Figure 10. The distribution and frequency of the target *hotspots* through (**a**) the whole year; (**b**) cold season of December–February; (**c**) warmer season of March–May; (**d**) hot season of June–August; and (**e**) cooler season of September–November.

Finally, a preliminary examination of the year-round *hotspots*-land surface composition relationship is conducted. The Terra MODIS Vegetation Continuous Field (VCF) product MOD44B of 2012 is used. The data contains yearly bare land, tree cover vegetation and non-tree cover vegetation percentage information. The bare land can either be an unvegetated built surface or bare soil and rocks. The data is validated through a field campaign [49]. The yearly bare land percentage is shown in Figure 11a, and the bare land proportion at the pixel level in built-up areas is mostly between 30% and 70%. When the yearly bare land percentage and the type I *hotspots* frequency in Figure 10a are considered together as shown in Figure 11b, it is clear that a positive correlation exists when the bare land percentage is roughly less than 70%. It means that the frequency of being type I *hotspot* through the year is potentially and positively correlated to its bare land percentage within the built-up area. As the relationship is unclear, a non-parametric Gaussian kernel regression is used to fit and highlight the potential trend. When the bare land percentage is greater than 70%, the trend vanishes. These places may be industrial plants or construction sites along the urban periphery with large portions of unvegetated land. They can also be characterized as type I *hotspots*. However, bare soil surface in the rural areas can hardly be considered as type I *hotspots*. This finding promotes further examination of such a relationship within the built-up area. Figure 11c shows that while the bare land percentage is less than 70% (the bare land-vegetation ratio is 2.33 or less), the average curvedness of the *hotspots* could be potentially influenced by the yearly bare land–vegetation interaction. When the bare land and vegetation cover in a pixel are roughly equal, the temperature pattern becomes less homogeneous, and the curvedness of the pattern in that pixel increases. The pixel might be located on a sharp edge of land type transition, which forces the LST changes to occur faster and the curvedness of the LST surface increases in the pixel. The trend is highlighted by the Gaussian kernel regression line. The findings again underlie how the land surface composition can govern the behavior of the *hotspots*.

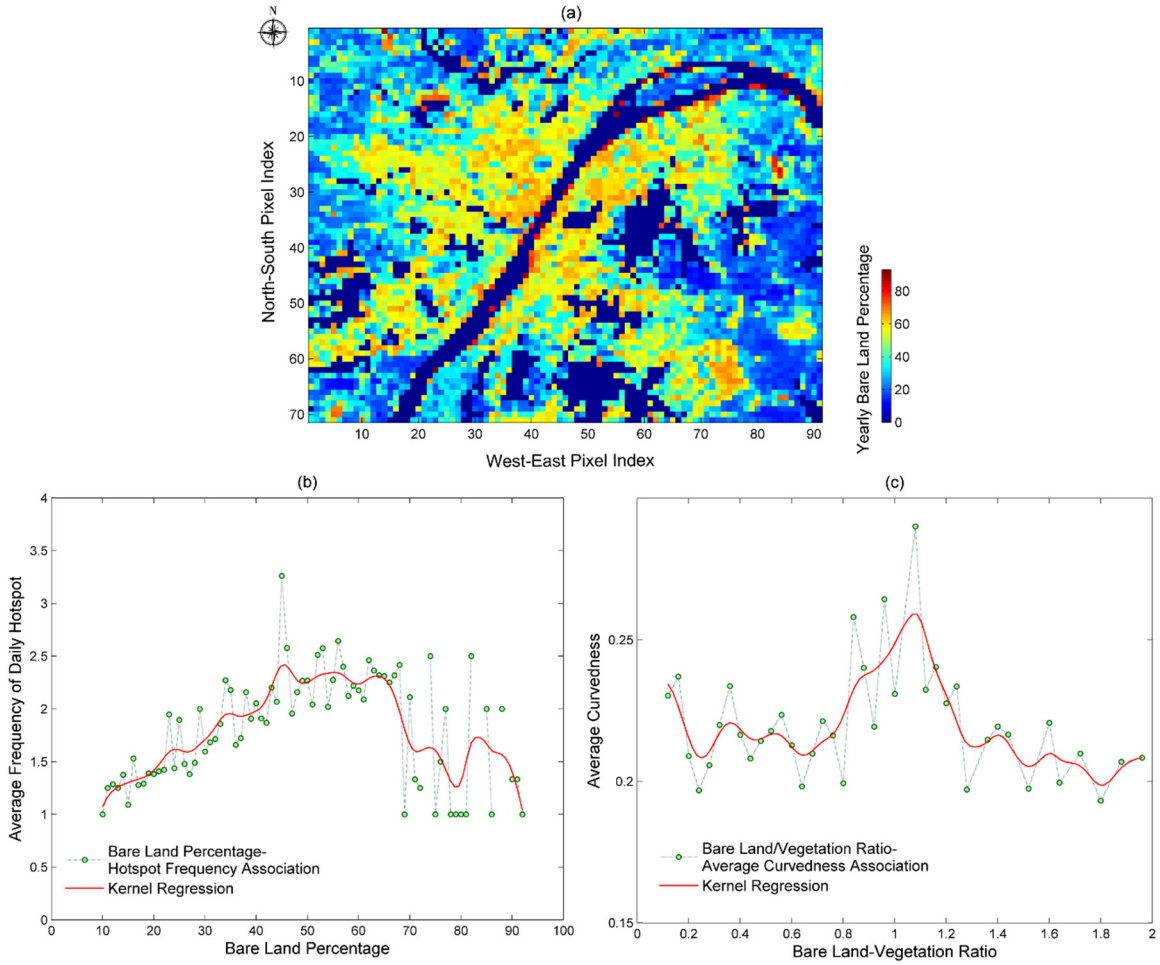

Figure 11. The *hotspot* dynamics–land surface composition relationship. (**a**) The yearly bare land percentage; (**b**) The yearly bare land percentage–*hotspots* frequency association. The frequencies are averaged in each 1-percent-interval of bare land to highlight the trend; (**c**) The impacts of bare land-vegetation cover ratio on the *hotspots* curvedness. The curvedness are averaged in each 0.04 of the ratio interval to highlight the trend.

4. Discussion

This research involves the investigation of temperature phenomenon, the model configuration, as well as the potential application of the findings in the planning domain. The research intends to provide an interface between the study of this phenomenon and planning strategies. Several theoretical and technical issues are worth discussing.

4.1. The Scale of Investigation

The temperature as a geographic phenomenon is with no exception governed by scale. Such research constantly involves determining the level of study and observational and operational scales [50,51]. The issue of scale in this study is manifold. The study is claimed to be at local scale relative to conventional temperature studies at city scale. This scale is only a rough guideline that defines the level of research. The scale considers that the city holistically is defined as city scale, while the districts or communities within a city are at local or even micro scale. A more rigorous adoption of scale lies in the application of the MSSI to the detection of the features at the optimal scale. This scale corresponds to the scale at which local features essentially come into focus.

4.2. Phenomena Study and the Planning Profession

The problem of scale partially contributes to the creation of the barrier between meteorology research and the planning profession. The research of temperature patterns within and around urban areas has been carried out for years. Most of the studies focus on the citywide scale. Such approach remains unchanged for nearly 180 years [28]. The findings from meteorological research can hardly meet the needs of planning professionals.

It has been noted earlier that studies would continue to focus for a long period of time on phenomena recognition and description before drawing any relationships [5]. This might be a potential reason that researchers are unaware of planners' needs. Needs-oriented studies are highly encouraged in future meteorological and environmental research. Issues including scales, zones, and hierarchies can be considered in the early stage of phenomena characterization.

4.3. The Indicators for Characterizing LST Patterns

The issue of scale also induces the problem of indicators for characterizing the LST pattern. The indicators applied in previous studies at city scale [18] such as magnitude, range, and gradient implicitly oversimplified the spatial character of urban areas. These indicators are all based upon the premise that cities can be delineated by the "urban–rural" dichotomy. They failed to capture the diversity of urban phenomena.

The strength of the MSSI or the triplet of criteria (the MSSI, curvedness/scale, and temperature) is threefold. Firstly, it helps to capture the diversity of the LST pattern which underlies urban heterogeneity. Secondly, it acts as an interface where meteorological findings can be better applied in the planning profession. Thirdly, it adds a spatial or morphological dimension to the study of temperature patterns. According to the results, temperature variations can be quite similar whereas the deformations are quite different.

4.4. Understanding the Urban Environmental Process

A process-based understanding of LST dynamics creates challenges in drawing relationships between the phenomena and land surface specification. Both the LST and land surface composition are by no means static [52,53]. The strength and scale of the relationship may vary, which leads to further uncertainties in mitigation and adaptation strategies. Yet, plans should be more efficient.

4.5. Hypothesis, Model Feasibility and Data

One last issue to be addressed is the techniques applied in this research. The major difference between the LST pattern research and other meteorological studies is the spatial coverage of the source data. Such spatial abundance promotes visual interpretation and facilitates the establishment of a hypothesis. The data coverage not only specifies the model type more clearly, but also ensures the application of some flexible models. In contrast, the Gaussian Process model could be applied to air temperature pattern study, but the sparsity and uncertainty of the data may undermine the flexibility of the model to some extent. In fact, the reliability of this study is ultimately restricted by the uncertainty of satellite image data despite its spatial coverage. The accuracy of the satellite image data is inevitably affected by the roughness of the land surface and the direction of image acquirement [16,54]. The directional variation of the measured temperature can be intensified by built-up surface areas, such as business, residential and industrial districts. Thus, the anisotropy of temperature measurements may bring serious uncertainties to the image data [10]. Besides, short term weather conditions may also affect the reliability of the modeling. Even though the MODIS data is validated through field campaigns, the derivation of LST may still be influenced by the uncertainty of atmospheric, astronomical and meteorological parameters [54].

5. Conclusions

A procedure for analyzing the LST pattern and identifying the *hotspots* at a local scale around urban areas is presented. The scope of this research may potentially facilitate collaboration between the climate research field and the planning profession. The identification of the *hotspots* in terms of types helps to determine areas of priority for the implementation of mitigation and adaptation strategies. This is practical for planning.

In the examination of the local LST deformation, the MTGP model appears to be a reliable approach to first determine the continuous smooth latent LST pattern. The determination gives statistically robust results. Such a smooth continuous surface successively helps to apply the MSSI and related criteria to characterize the morphological features of the latent LST. The MSSI, curvedness/scale, and temperature then act as a triplet of criteria to investigate the deformation of the latent LST for days and seasons. Those places with the most critical deformations over time are finally identified as *hotspots*.

The *hotspots* in conjunction with their transition types provide intrinsically dynamic information. Firstly, they provide an idea of how latent LST deforms at a local scale over time. Secondly, they show the intensity of deformation in terms of shape, and scale/curvedness. The MSSI and scale/curvedness add an important spatial or morphological dimension to the temperature analysis. Thirdly, the morphological behaviors of the *hotspots* confirm the fact that places surrounding built-up areas may demonstrate different characteristics to rural surroundings. Lastly, the morphological criteria facilitate the analysis of the relationship between the LST pattern and land surface composition. Such spatial or morphological characterization of the LST provides insights into how land surface factors govern the dynamics of the LST as well as the *hotspots* at a local scale.

The dynamics explored in this research, on one hand, presents the opportunity to apply climate research in the planning domain. On the other hand, such dynamics may also make it more difficult to determine a clear relationship between various phenomena and land surface factors. Research incorporating high temporal resolutions at a local scale is highly needed in future studies.

Acknowledgments: This research is supported by the National Natural Science Foundation of China (51378399, 41331175).

Author Contributions: Jiong Wang proposed the research concept, designed the experiments, conducted data analysis, and composed the manuscript. Qingming Zhan is responsible for framework design of this research and participated in data validation and manuscript editing. Huagui Guo participated in the data preparation and analysis.

Conflicts of Interest: The authors declare no conflict of interest.

References

1. Stone, B. Urban and rural temperature trends in proximity to large us cities: 1951–2000. *Int. J. Clim.* **2007**, *27*, 1801–1807. [CrossRef]
2. Manley, G. On the frequency of snowfall in metropolitan england. *Q. J. R. Meteorol. Soc.* **1958**, *84*, 70–72. [CrossRef]
3. Landsberg, H.E. *The Urban Climate*; Academic Press: New York, NY, USA, 1981; Volume 28.
4. Oke, T.R. Canyon geometry and the nocturnal urban heat island: Comparison of scale model and field observations. *J. Clim.* **1981**, *1*, 237–254. [CrossRef]
5. Oke, T.R. The energetic basis of the urban heat island. *Q. J. R. Meteorol. Soc.* **1982**, *108*, 1–24. [CrossRef]
6. Howard, L. *The Climate of London: Deduced from Meteorological Observations Made in the Metropolis and at Various Places Around It*; Harvey and Darton: London, UK, 1833; Volume 2.
7. Oke, T.R. The distinction between canopy and boundary-layer urban heat islands. *Atmosphere* **1976**, *14*, 268–277.
8. Kalnay, E.; Cai, M. Impact of urbanization and land-use change on climate. *Nature* **2003**, *423*, 528–531. [CrossRef] [PubMed]

9. Stone, B.; Vargo, J.; Habeeb, D. Managing climate change in cities: Will climate action plans work? *Landsc. Urban. Plan.* **2012**, *107*, 263–271. [CrossRef]
10. Voogt, J.A.; Oke, T.R. Thermal remote sensing of urban climates. *Remote Sens. Environ.* **2003**, *86*, 370–384. [CrossRef]
11. Li, Z.-L.; Tang, B.-H.; Wu, H.; Ren, H.; Yan, G.; Wan, Z.; Trigo, I.F.; Sobrino, J.A. Satellite-derived land surface temperature: Current status and perspectives. *Remote Sens. Environ.* **2013**, *131*, 14–37. [CrossRef]
12. Anderson, M.; Norman, J.; Kustas, W.; Houborg, R.; Starks, P.; Agam, N. A thermal-based remote sensing technique for routine mapping of land-surface carbon, water and energy fluxes from field to regional scales. *Remote Sens. Environ.* **2008**, *112*, 4227–4241. [CrossRef]
13. De Kauwe, M.G.; Taylor, C.M.; Harris, P.P.; Weedon, G.P.; Ellis, R.J. Quantifying land surface temperature variability for two sahelian mesoscale regions during the wet season. *J. Hydrometeorol.* **2013**, *14*, 1605–1619. [CrossRef]
14. Sobrino, J.; Oltra-Carrió, R.; Sòria, G.; Bianchi, R.; Paganini, M. Impact of spatial resolution and satellite overpass time on evaluation of the surface urban heat island effects. *Remote Sens. Environ.* **2012**, *117*, 50–56. [CrossRef]
15. Roth, M.; Oke, T.; Emery, W. Satellite-derived urban heat islands from three coastal cities and the utilization of such data in urban climatology. *Int. J. Remote Sens.* **1989**, *10*, 1699–1720. [CrossRef]
16. Voogt, J.A.; Oke, T.R. Complete urban surface temperatures. *J. Appl. Meteorol.* **1997**, *36*, 1117–1132. [CrossRef]
17. Weng, Q. Thermal infrared remote sensing for urban climate and environmental studies: Methods, applications, and trends. *ISPRS J. Photogramm. Remote Sens.* **2009**, *64*, 335–344. [CrossRef]
18. Schwarz, N.; Schlink, U.; Franck, U.; Großmann, K. Relationship of land surface and air temperatures and its implications for quantifying urban heat island indicators—An application for the city of leipzig (germany). *Ecol. Indic.* **2012**, *18*, 693–704. [CrossRef]
19. Streutker, D.R. A remote sensing study of the urban heat island of houston, Texas. *Int. J. Remote Sens.* **2002**, *23*, 2595–2608. [CrossRef]
20. Streutker, D.R. Satellite-measured growth of the urban heat island of houston, Texas. *Remote Sens. Environ.* **2003**, *85*, 282–289. [CrossRef]
21. Rajasekar, U.; Weng, Q. Urban heat island monitoring and analysis using a non-parametric model: A case study of Indianapolis. *ISPRS J. Photogramm. Remote Sens.* **2009**, *64*, 86–96. [CrossRef]
22. Wheeler, S.M. State and municipal climate change plans: The first generation. *J. Am. Plan. Assoc.* **2008**, *74*, 481–496. [CrossRef]
23. Betsill, M.; Rabe, B. Climate change and multilevel governance: The evolving state and local roles. In *Toward Sustainable Communities: Transition and Transformations in Environmental Policy*; MIT Press: Cambridge, MA, USA, 2009.
24. Griggs, D.J.; Noguer, M. Climate change 2001: The scientific basis. Contribution of working group i to the third assessment report of the intergovernmental panel on climate change. *Weather* **2002**, *57*, 267–269. [CrossRef]
25. Valleron, A.; Boumendil, A. Epidemiology and heat waves: Analysis of the 2003 episode in France. *Comptes Rend. Biol.* **2004**, *327*, 1125–1141. [CrossRef]
26. Prevention. Heat-related mortality—Arizona, 1993–2002, and united states, 1979–2002. *Morb. Mortal. Wkly. Report* **2005**, *54*, 628–630.
27. Kalkstein, L.; Koppe, C.; Orlandini, S.; Sheridan, S.; Smoyer-Tomic, K. Health impacts of heat: Present realties and potential impacts of climate change. In *Distributional Impacts of Climate Change and Disasters*; Edward Elgar: Cheltenham, UK, 2009; pp. 69–81.
28. Stewart, I.D. A systematic review and scientific critique of methodology in modern urban heat island literature. *Int. J. Clim.* **2011**, *31*, 200–217. [CrossRef]
29. Chang, C.-R.; Li, M.-H.; Chang, S.-D. A preliminary study on the local cool-island intensity of taipei city parks. *Landsc. Urban Plan.* **2007**, *80*, 386–395. [CrossRef]
30. Eliasson, I. The use of climate knowledge in urban planning. *Landsc. Urban Plan.* **2000**, *48*, 31–44. [CrossRef]
31. Arnfield, J. Two decades of urban climate research: A review of turbulence exchanges of energy and water, and the urban heat island. *Inter. J. Clim.* **2003**, *23*, 1–26. [CrossRef]

32. Quan, J.; Chen, Y.; Zhan, W.; Wang, J.; Voogt, J.; Wang, M. Multi-temporal trajectory of the urban heat island centroid in Beijing, China based on a gaussian volume model. *Remote Sens. Environ.* **2014**, *149*, 33–46. [CrossRef]
33. Wan, Z.; Dozier, J. A generalized split-window algorithm for retrieving land-surface temperature from space. *IEEE Trans. Geosci. Remote Sens.* **1996**, *34*, 892–905.
34. Wan, Z.; Zhang, Y.; Zhang, Q.; Li, Z.-L. Quality assessment and validation of the modis global land surface temperature. *Inter. J. Remote Sens.* **2004**, *25*, 261–274. [CrossRef]
35. Wan, Z. New refinements and validation of the MODIS land-surface temperature/emissivity products. *Remote Sens. Environ.* **2008**, *112*, 59–74. [CrossRef]
36. Wan, Z. New refinements and validation of the collection-6 modis land-surface temperature/emissivity product. *Remote Sens. Environ.* **2014**, *140*, 36–45. [CrossRef]
37. Pasquill, F.; Smith, F. *Atmospheric Diffusion: Study of the Dispersion of Windborne Material from Industrial and other Sources*; John Wiley & Sons: New York, NY, USA, 1983.
38. Tomlinson, C.; Chapman, L.; Thornes, J.; Baker, C. Derivation of Birmingham's summer surface urban heat island from MODIS satellite images. *Int. J. Clim.* **2012**, *32*, 214–224. [CrossRef]
39. Chapman, L.; Thornes, J.E.; Bradley, A.V. Modelling of road surface temperature from a geographical parameter database. Part 1: Statistical. *Meteorol. Appl.* **2001**, *8*, 409–419. [CrossRef]
40. Goodchild, M.F. A spatial analytical perspective on geographical information systems. *Int. J. Geogr. Inf. Syst.* **1987**, *1*, 327–334. [CrossRef]
41. Goodchild, M.F. Integrating GIS and remote sensing for vegetation analysis and modeling: Methodological issues. *J. Veg. Sci.* **1994**, *5*, 615–626. [CrossRef]
42. Bonilla, E.V.; Chai, K.M.; Williams, C. Multi-task gaussian process prediction. In *Advances in Neural Information Processing Systems*; Donnelley & Sons: San Francisco, CA, USA, 2008.
43. Rasmussen, C.E. Gaussian Processes for Machine Learning. In *Advanced Lectures on Machine Learning*; Springer: Heidelberg, Germany, 2004; pp. 63–71.
44. Blumer, A.; Ehrenfeucht, A.; Haussler, D.; Warmuth, M.K. Occam's razor. *Inf. Proc. Lett.* **1987**, *24*, 377–380. [CrossRef]
45. Bonde, U.; Badrinarayanan, V.; Cipolla, R. *Multi Scale Shape Index for 3D Object Recognition*; Springer: Heidelberg, Germany, 2013.
46. Koenderink, J.J.; van Doorn, A.J. Surface shape and curvature scales. *Imag. Vis. Comput.* **1992**, *10*, 557–564. [CrossRef]
47. Lindeberg, T. Feature detection with automatic scale selection. *Int. J. Comput. Vis.* **1998**, *30*, 79–116. [CrossRef]
48. Lowe, D.G. Object recognition from local scale-invariant features, computer vision. *Proc. IEEE* **1999**, *2*, 1150–1157.
49. DiMiceli, C.; Carroll, M.; Sohlberg, R.; Huang, C.; Hansen, M.; Townshend, J. *Annual Global Automated Modis Vegetation Continuous Fields (Mod44b) at 250 m Spatial Resolution for Data Years beginning Day 65, 2000–2010, Collection 5 percent Tree Cover*; University of Maryland: Maryland, MD, USA, 2011.
50. Sayre, N.F. Ecological and geographical scale: Parallels and potential for integration. *Prog. Hum. Geogr.* **2005**, *29*, 276–290. [CrossRef]
51. Sayre, N.F. Scale. *Wiley Online Libr.* **2009**. [CrossRef]
52. Rizwan, A.M.; Dennis, L.Y.; Liu, C. A review on the generation, determination and mitigation of urban heat island. *J. Environ. Sci.* **2008**, *20*, 120–128. [CrossRef]
53. Zhou, D.C.; Zhao, S.Q.; Liu, S.G.; Zhang, L.X.; Zhu, C. Surface urban heat island in China's 32 major cities: Spatial patterns and drivers. *Remote Sens. Environ.* **2014**, *152*, 51–61. [CrossRef]
54. Podobnikar, T.; Ostir, K.; Zaksek, K. Influence of data quality on solar radiation modeling. In *Gis for Sustainable Development*; Campagna, M., Ed.; CRC Press, Taylor & Francis Group: Boca Raton, FL, USA, 2006; pp. 417–430.